

Automatic Defect Detection in Epitaxial Layers by Micro Photoluminescence Imaging

Jacopo Frascaroli^{ID}, Marta Tonini^{ID}, Selene Colombo, Luisito Livellara, Luca Mariani, Paolo Targa, Roberto Fumagalli, Viktor Samu, Máté Nagy, Gábor Molnár, Áron Horváth, Zoltán Bartal, Zoltán Kiss, Tamás Sipőcz, and Isabella Mica^{ID}

Abstract—The early in-line detection of defects is a fundamental step in semiconductor manufacturing to ensure the device quality. Inspection techniques currently available can effectively detect large epitaxial defects causing morphological surface variations like stacking faults, while dislocations go undetected. Herein we introduce a new technology with enhanced machine learning analysis, based on contactless and non-destructive room temperature micro-photoluminescence imaging (micro-PL), for the detection and classification of defects in silicon epitaxial layers. With laboratory microscopy techniques we investigate the correspondence between different defect morphologies in micro-PL images and extended crystallographic defects. A good matching in terms of defect density is found between automatic micro-PL analysis and the standard laboratory analysis in an interval spanning from few defects/cm² up to 10⁵ defects/cm².

Index Terms—Photoluminescence, silicon epitaxial layers, crystal defects, artificial neural networks, image segmentation.

I. INTRODUCTION

EPITAXIAL layer growth is one of the most fundamental techniques of semiconductor manufacturing. The fact that the epitaxial layer grows in a well-ordered manner gives the opportunity of fine-tuning the wafer surface properties and the thickness of the epitaxial layer itself through the control of the growth parameters [1], [2].

During the epitaxial layer growth, the silicon atoms are joining the substrate's crystal lattice undisturbed. However, foreign particles on the substrate or irregularities near the surface cause mismatch in the epitaxial crystal structure leading to defective areas [3], [4]. Another challenge is the epitaxial growth on high doped layers to produce buried layers. Indeed, the recovery of the implantation damage is crucial to obtain a good quality of the epitaxial layer. As the manufacturing

cost of a completely clean substrate, thus a defectless epitaxial layer, would be beyond reason, defects are considered as part of the process and their characterization is mandatory.

Irregularities influence the device performance [5]–[7], therefore numerous techniques were developed to investigate the defectiveness of epitaxial layers [8], [9]. If the defects produce a surface morphology, defect inspection techniques such as surface light scattering or Nomarski optical interference contrast allow the detection of defects [10], [11]. However, if the defect lies just below the surface or if the defect dimensions do not allow a surface detection, only destructive methods were available so far, including TEM and chemical etching techniques [12] coupled with optical microscopy or SEM that give information only on the near surface region of the semiconductor. Additionally, in case of buried defects, the wafer must be cleaved for an investigation in deeper regions and the measurements become time consuming and expensive. Therefore, these methods are not suitable for in-line production analysis and monitoring.

Herein, we describe a non-destructive, non-contact and fast optical metrology based on photoluminescence (PL) emission from epitaxial defects when excess carriers are generated by external excitation [13], [14]. Data acquisition occurs at room temperature (RT), thus avoiding wafer cooling and speeding-up the measurement time. The measurement system provides PL images of the radiative recombination through crystal defects and allows the classification of defects based on their shape, intensity, and emission band. Additionally, Artificial Neural Networks (NN) were applied for the on-line analysis of PL images, resulting in a fully automated inspection and defect classification. Using this analysis, different defect types can be distinguished and characterized based on a user-defined and trained dataset. With the help of the NN the prediction of defect-dependent device performance, therefore the whole production optimization can be speeded up.

The purpose of this study is to investigate the potential, the reliability, and the performance of the RT micro-PL imaging coupled with a NN as an in-line, automatic analysis tool.

II. EXPERIMENTAL

A. RT Micro-PL Imaging Setup

The RT PL imaging system was provided by Semilab Ltd. Semiconductor Physics Laboratory with commercial name En-Vision 3000. The technique is based on the inspection of

Manuscript received 7 April 2022; revised 10 June 2022; accepted 6 July 2022. Date of publication 11 July 2022; date of current version 4 August 2022. This work was supported in part by the Electronic Components and Systems for European Leadership-Joint Undertaking (ECSEL-JU) through the Project Metrology Advances for Digitized Electronic Components and Systems Industry 4.0 (MADEin4) under Grant 826589. (Corresponding author: Jacopo Frascaroli.)

Jacopo Frascaroli, Marta Tonini, Selene Colombo, Luisito Livellara, Luca Mariani, Paolo Targa, and Isabella Mica are with STMicroelectronics, 20864 Agrate Brianza, Italy (e-mail: jacopo.frascaroli@st.com).

Roberto Fumagalli, Viktor Samu, Máté Nagy, Gábor Molnár, Áron Horváth, Zoltán Bartal, Zoltán Kiss, and Tamás Sipőcz are with Semilab Semiconductor Physics Laboratory Company Ltd., 1117 Budapest, Hungary.

Color versions of one or more figures in this article are available at <https://doi.org/10.1109/TSM.2022.3189847>.

Digital Object Identifier 10.1109/TSM.2022.3189847

PL emission peaks of silicon, specifically: a) direct radiative recombination from silicon conduction band to silicon valence band (band-to-band PL) and b) radiative recombination through crystal defects (defect-band PL). Both band-to-band and defect-band PL signals are in the Near Infra-Red wavelength range (NIR).

Since silicon is an indirect gap semiconductor, the power density of its band-to-band PL is orders of magnitude lower compared to the excitation, and the defect-band PL signal is even few orders of magnitude lower than the band-to-band PL, which makes it challenging to be observed. To do so, the system relies on the use of bandpass optical filters coupled to a high sensitivity camera operating in the NIR wavelength range. This establishes a major difference with conventional PL systems which are usually based on a high-resolution spectrometer coupled to a single point detector or a bar detector. Consequently, the PL wavelengths observed by the PL imaging setup are integrated by the camera over the selected filter range (band-to-band or defect-band). This approach helps to enhance signal to noise ratio when working at RT. Although the individual D-lines cannot be resolved, combination of optical filtering with PL imaging provides sufficient information about defect types and defect density for in-line quality control in the semiconductor device production industry [15].

The RT micro-PL setup used enables fast acquisition of PL images with magnification up to 100X, corresponding to a field of view of $140 \times 175 \mu\text{m}^2$ in a single shot. For this experiment the PL measurements were acquired focusing at the surface with a 49.716 mW LASER power, 300 ms exposure time and image averaging set to 15, at highest magnification (100X, $1 \mu\text{m}$ resolution). The emitted light was filtered with a 1400 nm long pass filter.

B. Selective Defect Etch – Scanning Electron Microscopy (SEM) and Optical Inspection

Crystal defects were identified at the sample surface using optical microscopy or SEM after defects themselves were made visible at the silicon surface by an anisotropic chemical etching. Secco d'Aragona is an aqueous solution containing $\text{K}_2\text{Cr}_2\text{O}_7$ and HF. This solution has a higher etching rate for the atoms along the dislocation lines compared to atoms constituting the crystallographic plane of the silicon wafer [12]. The etch pits and surface grooves delineated by the Secco etching are proportional to the size of the extended crystal defects, which propagate to the surface. The analysis is possible either on the wafer surface or in depth after the cleavage of the wafer and the cross-section etching. The Optical Microscope used for the analyses is the Leica DM12000M, which is equipped with Differential Interference Contrast acquisition method. The SEM tool used for measurements is the Zeiss Ultra55.

C. Transmission Electron Microscopy (TEM)

For further comparison and more detailed defect inspection TEM has also been utilized. Specifically, the FEI TECNAI TF30 where the source is a Field Emission Gun is the

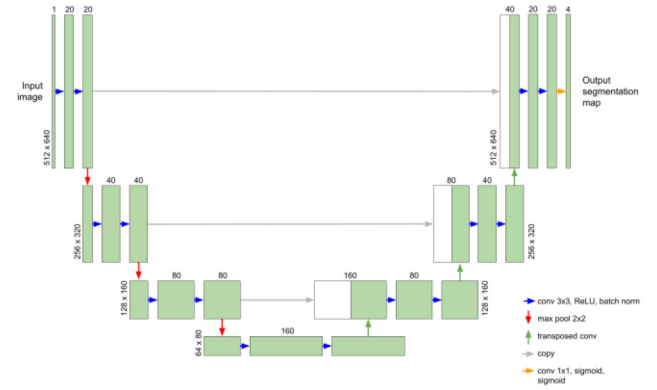


Fig. 1. U-net architecture of the convolutional neural network used for the automatic detection and classification of defects in the epitaxial layer.

equipment used for the analyses of the paper. The tool allows the Scanning TEM mode (STEM).

D. Automatic Defect Detection

Artificial neural networks (NNs) have been successfully applied in the semiconductor industry for defect detection and classification [16]–[18]. The En-Vision system carries out a pixelwise defect detection, defect counting is implemented as a separate step from the NN. Therefore the system applies an image segmentation NN.

Many NN architectures have been investigated in the recent years for the task of image segmentation, such as FCN24, SegNet25 and U-net [19]. The En-Vision system uses a variant of the U-net [20] architecture (Fig. 1), the most common architecture for image segmentation. Instead of unpadded convolutions, our modified architecture uses padded convolutions. At the final layer after the 1×1 convolutions a sigmoid activation function is added. Batch normalization is applied after each ReLU [21]. Feature counts by layer are 20, 40, 80 and 160, respectively. For detecting epi defects a narrow receptive field is enough as these defects are rather simple, small, and independent, thus we do not need a deep network.

For training the network, the Adam optimizer [22] with 0.001 learning rate was applied. The loss function was focal loss [23], while the batch size was set to 1. Training per validation set count ratio was 80/20. To avoid the overfitting during the training, an early stopping method was applied: the training session was stopped when the validation error did not improve in the last 100 epochs, and the state with the lowest validation error was returned.

III. SAMPLE PREPARATION

Epitaxial defects were generated by growing an epitaxial layer on Sb implanted samples with a not well recovered implant damage and oversaturated Sb content. The sample preparation consisted of screen oxide growth, Sb ion implantation, furnace annealing in a N_2/O_2 mixed environment, oxide removal and epitaxial growth. The Sb implant energy and the annealing temperature were varied to scale the defect density over several orders of magnitude.

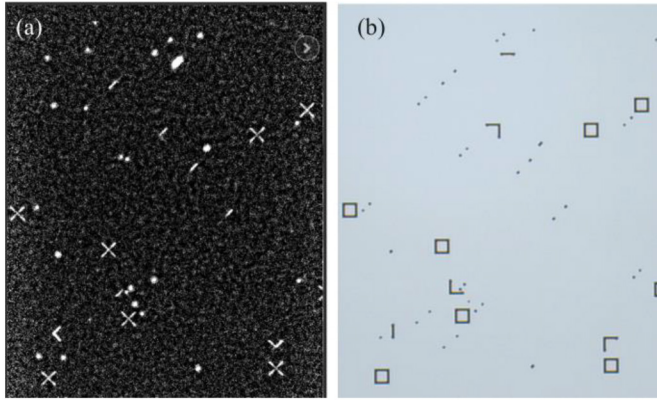


Fig. 2. (a) RT micro-PL image acquired at highest magnification (100X optics) and (b) same sample area imaged by optical microscopy after preferential etch of the epitaxial defects.

The inspection point for the micro-PL analysis was after epitaxial growth. No pattern was present in the areas inspected and the PL signal came only from epitaxial defects.

IV. RESULTS AND DISCUSSION

The growth of an epitaxial layer on top of previously implanted areas is especially critical since a not complete recovery of the silicon before growth leads to crystallographic defects. For this reason, epitaxial layers grown on Sb-implanted areas were chosen as test vehicle to evaluate the performance of RT micro-PL imaging to recognize and classify epitaxial defects. A variety of crystallographic defects can be formed with different extensions, namely dislocations and epitaxial stacking faults (ESFs).




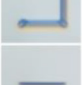

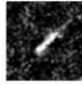

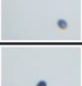
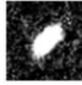



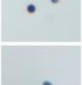
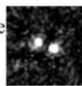
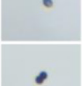


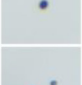

A. Detection of Epitaxial Defects by Micro-PL Imaging and Comparison With Selective Defect Etch Technique

First, the ability of RT micro-PL imaging to detect epitaxial defects on Sb-implanted areas was evaluated in comparison with preferential defect etch at the surface, which is the standard reference technique. As opposed to RT micro-PL imaging, defect etch is a destructive technique performed in the laboratory.

An example of an RT micro-PL image is reported in Fig. 2(a). Based on their shapes in the acquired PL images, defects were divided into five classes: crosses, half crosses, lines, thick lines, and points or double points. These classes are only phenomenological, but an actual correspondence with crystallographic defects will be discussed later in the paper. In Fig. 2(b) an image of the same area was acquired by optical microscopy after preferential defect etch. Stacking faults produce linear grooves on the surface when etched, while dislocations form an etch pit at the point where the dislocation emerges on the etched surface.

The direct comparison illustrated in Fig. 2 proved to us that RT micro-PL imaging has the physical ability to detect these epitaxial defects. However, note that preferential etch can only highlight defects which reach the top surface, while PL emission also occurs from defects buried in the silicon within

TABLE I
MATCHING OF DEFECT SHAPES BETWEEN MICRO-PL IMAGES
AND DEFECT ETCH AT SURFACE

Class	Micro-PL	Preferential defect etch	Matching	Defect type
A	Cross 	Square 	100%	Stacking fault
B	Half cross 	Half square 	33.3%	Stacking fault
		Line 	66.7%	Stacking fault
C	Line 	Half square 	24.2%	Stacking fault
		Double point 	75.8%	Dislocation
D	Thick line 	Big spot 	75%	Dislocation
		Line 	25%	Stacking fault
E	Point 	Double point 	64.2%	Dislocation
	Double point 	Single point 	32.1%	Dislocation
		Double point 	3.8%	Dislocation
	Point 	Defect not detected with preferential etch	24.3%*	Dislocation
	Defect not detected with micro-PL	Single point 	6.9%*	Dislocation
		Double point 	2.1%*	Dislocation

*Percentage out of the total number of defects observed by both techniques combined

the epitaxial layer. This is also the reason why defects appear with very different shapes with the two techniques.

To compare the two analysis techniques, ten different measurement sites were compared for a total analysis area of $2.45 \cdot 10^5 \mu\text{m}^2$. The result of this one-to-one comparison is summarized in Table I. A matching percentage is provided for the correspondence between the five defect classes identified in micro-PL images and the corresponding shapes at surface after defect etch. A 100% matching is only found between micro-PL crosses and square grooves. These are well known pyramidal defects with an origin located at the bottom of the epitaxial layer and four ESFs as the sides of this pyramid. Micro-PL half crosses, while corresponding to different groove shapes, can always be interpreted as coming from ESFs. The same is true for point-like features in PL images, which are always

produced by dislocations, albeit their respective shapes after etching can differ. In contrast, micro-PL lines and thick lines can match either with grooves or point-like shapes after surface etch, meaning that a line-shaped micro-PL feature can be caused either by an ESF or a dislocation.

Not all the epitaxial defects are captured by both techniques, considering point-like defects in particular. An example can be seen in the upper left corner of Fig. 2(a), where four PL spots do not have any matching etch mark in Fig. 2(b). Overall, the portion of defects detected only in micro-PL images is about 24%, which is larger than the 9% of defects visible only after surface etching. An explanation could be found in the greater depth of capture of the PL signal. This way PL measurements allow to probe even those dislocations that remain buried and do not reach the surface during the etching process. On the other hand, some other defects probably do not produce a sufficient PL signal to emerge from the background in the micro-PL image.

B. Insight Into Defect Types Identified by PL Imaging at RT

TEM analysis was carried out for some defect types to identify the crystal defects corresponding to the defect shapes observed in micro-PL images (Fig. 3).

The TEM cross section image in Fig. 3(a) shows the tip of the inverted pyramid at a depth equal to the epitaxial layer thickness. Indeed, this confirms that cross-shaped micro-PL defects correspond to full pyramidal ESFs. When the defect is etched at the sample surface, square grooves appear where the four ESF planes cross the surface, at the base of the pyramid.

In Fig. 3(b) a half-cross micro-PL defect cut along the middle also shows an ESF originating at the bottom of the epitaxial layer. However, only half of the pyramid is present in this case. Consequently, two sides of the pyramid base square are visible at surface after etching. This means that PL emission occurs only from two of the three edges of the half-pyramid.

Lines in micro-PL images, as already observed, can be produced by either ESFs or dislocations aligned in the image plane. In Fig. 3(c) a micro-PL line corresponding to half square grooves after surface etch was cut and analyzed by TEM. Two ESFs appear in the TEM image, similarly to the previous case. This means that only one edge of the half pyramid is captured by the PL image. In Fig. 3(d) a micro-PL line corresponds to two etch pits at the surface. In this case, the TEM lamella was cut at 45° angle in order to contain both etch pits. The analysis reveals not an ESF but two dislocations with common origin at the bottom of the epitaxial layer. These dislocations follow the same slip planes of ESFs found in the other examples. However, dislocations can have various shapes and are not necessarily aligned along preferential directions. For example, two cases are reported here; in Fig. 3(e), where etch pits are not situated at a 45° angle and have different shapes, and in Fig. 3(f), where only one big etch pit was found. TEM analysis reveals in both cases that two dislocation lines originating at the bottom of the epitaxy are propagating to the surface with different angles and relative distance. Indeed, the large etch pit of Fig. 3(f) corresponds to two very close dislocation tips at the surface.

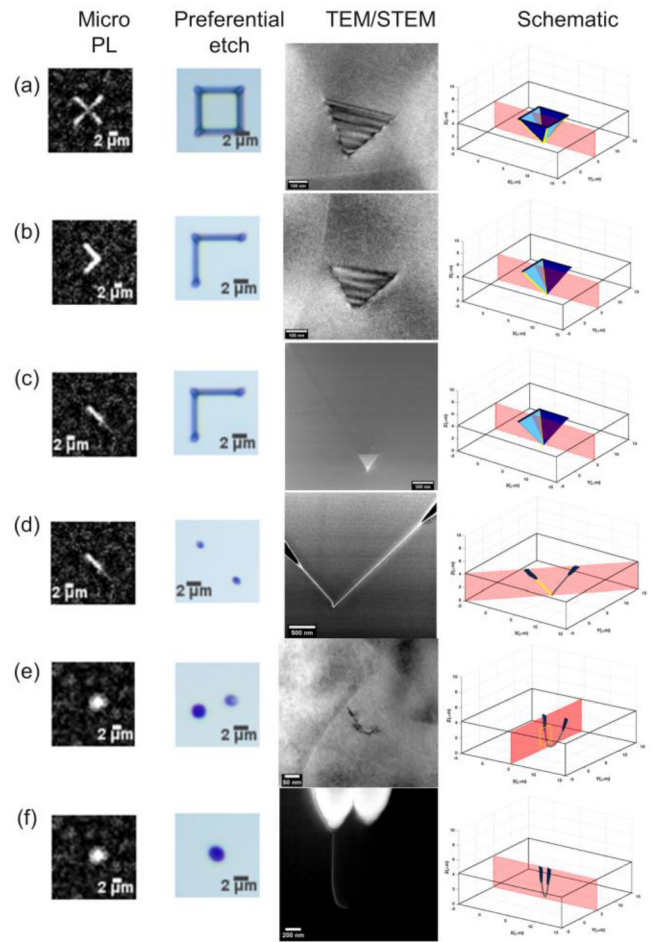


Fig. 3. (a)-(f) crystallographic defects observed, from left: by micro-PL imaging; after preferential etch at surface; by TEM/STEM cross section. On the right, a schematic image of the various defect morphologies reported with the TEM lamella cutting plane indicated in pink.

C. Automatic Recognition and Classification of Defects

In the previous paragraphs the ability of micro-PL imaging at RT to detect epitaxial defects has been established. The application of micro-PL imaging in the production line requires an on-line automatic recognition system for defect detection and classification with minimum assistance from human personnel. For this purpose, a NN was trained to detect defects belonging to the five different classes.

A set of 300 images were annotated, 240 of which were used for training and 60 for validation to stop the training procedure. Images coming from samples with different defect densities were annotated and inserted in the training, from zero defects up to about 30 defects per field of view. Overall, thousands of defects were annotated. Generally, 100,000 iterations are enough to train the network, which takes about 5 hours. The prediction time is 50 ms using an Nvidia RTX 1080 GPU.

The benchmark of the performance of defect detection and classification was performed using a twin test wafer with a similar defect density. 987 different fields of view with a total area of 0.242 cm², evenly distributed along the wafer surface, were acquired and analyzed using automatic classification. The same micro-PL images were then checked by

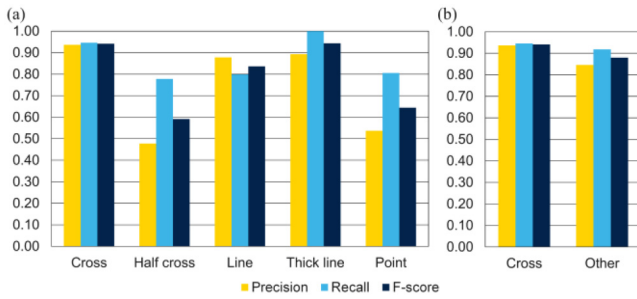


Fig. 4. Precision, recall and F-score rates of automatic recognition and classification of the epitaxial defects in micro-PL images for (a) five defect classes and (b) the defect classes other than crosses merged in a single defect class.

manual recognition to estimate the classification errors and accuracy. Overall, 1269 defects were detected by the NN and 1229 defects by manual count, with a 3.25% overcount. However, recognition accuracy varied greatly among classes. Recognition errors were distinguished as false positive, when the defect recognized by the NN was not actually present or should be assigned to a different class, and false negative, when the defect was not recognized or was assigned to another class. Since defect recognition was distinguished for each class, a misclassification returned two errors: one false negative for the correct class and one false positive for the wrong class.

In order to compare the recognition and error rates, the precision and recall rates, together with the F-score, are summarized in Fig. 4(a) for the five different classes. The precision rate accounts for the false positive results, while the recall rate accounts for the false negative results. The F-score, which is the harmonic mean of precision and recall, is used as a measure of the overall accuracy.

Crosses were the most easily detected defects, for which an F-score of 0.94 was achieved. This was due to their unique shape and of their high relative frequency in the training set. Indeed, crosses were the most common defect and constituted 77% of all the defects present in the test wafer. Moreover, crosses are the biggest epitaxial defects, which hamper the device the most when present and their detection is especially critical.

Concerning the other defect classes, the recognition accuracy expressed as F-score amounted to 0.59, 0.84, 0.94, and 0.64 for half crosses, lines, thick lines, and point, respectively. Overall, classification accuracy was hampered by the reduced dataset for training caused by the low frequency of these defects. Moreover, as already observed, the definition of these classes by shape is only phenomenological and an actual correspondence with physical defects is not bijective. For this reason, it makes sense to group these four classes together in a so-called “other defects” class which eliminates misclassification among these classes. If this integration is made, as reported in Fig. 4(b), an F-score of 0.88 is achieved.

In summary, good classification performance was obtained for the class of micro-PL crosses, which has an actual correspondence with full pyramidal ESF, and for the other, integrated class of all other defects, which are less frequent

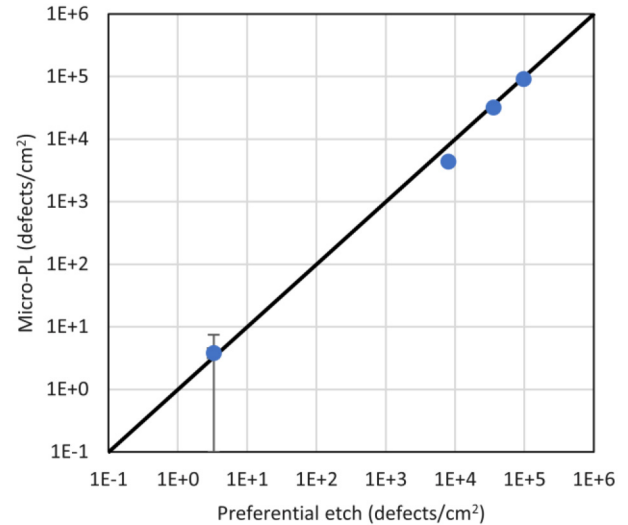


Fig. 5. Correlation of defect density observed by standard preferential etch technique compared with micro-PL imaging in samples with different Sb implant and annealing conditions.

epitaxial defects. It should be noted that the automatic classification was configured to catch the largest number of defects, since some false positives are tolerated in order to reduce the number of false negatives. Moreover, especially for small defects like point defects, the low detection accuracy was the result of a compromise between acquisition time and signal to noise ratio in the micro-PL images.

D. Extended Test Over a Wide Range of Defect Density

So far, the performance of the detection of epitaxial defects has been evaluated on a test wafer with a high defect density. As a further step, defect detection was explored on a set of wafers with varied Sb implant energy and annealing conditions prior to the epitaxial growth. These parameters allowed to produce samples with defect densities ranging from few defects/cm² to 10⁵ defects/cm². Moreover, these varied parameters yielded different relative ratios of the defect types. Defect count by micro-PL image acquisition and automatic recognition and classification was benchmarked with the standard preferential defect etching approach. The micro-PL acquisition consisted of 940 images per wafer, for a total area of 0.230 cm², while the area observed by optical microscopy varied between 0.016 cm² and 2 cm² depending on the observed defect density. It is worth noting that even for the highest defect density the defects do not overlap with each other significantly and the NN analysis can detect these defects individually.

The correlation between preferential etching and micro-PL analysis is reported in Fig. 5. A good correlation was found between the two techniques in the tested range, spanning over five orders of magnitude. While in most samples the variations between the two techniques are comprised within one standard deviation, a comparatively lower overall defect density is found in micro-PL images for the sample with a defect density in the 10³ – 10⁴ defects/cm² range.

V. CONCLUSION

Micro-photoluminescence imaging at room temperature allows an in-line, non-destructive and non-contact inspection of crystallographic defects generated during various semiconductor process steps. This work focuses on defect detection in epitaxial layer on Sb-implanted substrates generated by a not fully recovered Sb implant. The defect detection was first evaluated in comparison with a standard but destructive laboratory technique in which defects are preferentially etched in a solution. The defect matching between the two techniques is herein reported, finding that the micro-PL imaging can detect a comparatively larger percentage of epitaxial defects. For the main defect types, cross section TEM analysis allowed to determine the respective type and morphology of defects found by the micro-PL inspection. In order to setup an automatic detection and classification system, a neural network was trained to recognize defect images and tested on several wafers with different defect densities and relative defect quantities. Micro-PL image acquisition followed by automatic defect recognition and classification allowed to detect defects with a density spanning from few defects/cm² to 10⁵ defect/cm² with a good matching within the same order of magnitude compared to the standard laboratory technique followed by manual recognition. This work paves the way to a fast, completely automated and in-line detection of epitaxial defects in production wafers.

REFERENCES

- [1] H. Habuka, "Flatness deterioration of silicon epitaxial film formed using horizontal single-wafer epitaxial reactor," *Jpn. J. Appl. Phys.*, vol. 40, no. 10, p. 6041, 2001, doi: [10.1143/JJAP.40.6041](#).
- [2] M. Goulding, "The selective epitaxial growth of silicon," *J. Phys. IV*, vol. 2, no. C2, pp. 745–778, 1991, doi: [10.1051/jp4:1991290](#).
- [3] H. Aharoni, "Stacking faults in silicon epitaxial layers," *Vacuum*, vol. 26, nos. 4–5, pp. 167–180, 1976, doi: [10.1016/S0042-207X\(76\)80006-1](#).
- [4] S. Mahajan and K. S. S. Harsha, "Epitaxial growth," in *Principles of Growth and Processing of Semiconductors*, 1st ed. Singapore: McGraw-Hill, 1999, p. 26.
- [5] S. Mahajan, "Defects in semiconductors and their effects on devices," *Acta Mater.*, vol. 48, no. 1, pp. 137–149, 2000, doi: [10.1016/S1359-6454\(99\)00292-X](#).
- [6] A. K. Chin, "The effect of crystal defects on device performance and reliability," *J. Cryst. Growth*, vol. 70, nos. 1–2, pp. 582–596, 1984, doi: [10.1016/0022-0248\(84\)90320-8](#).
- [7] D. X. Xu, G. D. Shen, M. Willander, J. Knall, M.-A. Hasan, and G. V. Hansson, "The influence of defects on device performance of MBE-grown Si homojunction and strained Si_{1-x}Ge_x/Si heterostructures," *J. Electron. Mater.*, vol. 19, no. 10, pp. 1033–1041, 1990, doi: [10.1007/BF02651978](#).
- [8] V.-M. Airaksinen, "Chapter 7 epitaxial layer characterization and metrology," in *Silicon Epitaxy*, vol. 72, D. Crippa, D. L. Rode, and M. Masi, Eds. Burlington, VT, USA: Elsevier, 2001, pp. 225–276, doi: [10.1016/S0080-8784\(01\)80185-X](#).
- [9] M. H. Zoellner *et al.*, "Imaging structure and composition homogeneity of 300 mm SiGe virtual substrates for advanced CMOS applications by scanning X-ray diffraction microscopy," *ACS Appl. Mater. Interfaces*, vol. 7, no. 17, pp. 9031–9037, 2015, doi: [10.1021/am508968b](#).
- [10] A. J. Pidduck, D. J. Robbins, A. G. Cullis, D. B. Gasson, and J. L. Glasper, "In situ laser light scattering: I. Detection of defects formed during silicon molecular beam epitaxy," *J. Electrochem. Soc.*, vol. 136, no. 10, pp. 3083–3088, Oct. 1989, doi: [10.1149/1.2096405](#).
- [11] C. Dennis, R. Stanley, and S. Cui, "Detection of a new surface killer defect on starting Si material using Nomarski principle of differential interference contrast," in *Proc. IEEE/SEMI Adv. Semicond. Manuf. Conf.*, 2007, pp. 143–147, doi: [10.1109/ASMC.2007.375102](#).
- [12] F. S. d'Aragona, "Dislocation etch for (100) planes in silicon," *J. Electrochem. Soc.*, vol. 119, no. 7, p. 948, 1972, doi: [10.1149/1.2404374](#).
- [13] R. Duru *et al.*, "Photoluminescence for in-line buried defects detection in silicon devices," in *Proc. 28th Annu. SEMI Adv. Semicond. Manuf. Conf. (ASMC)*, 2017, pp. 262–266, doi: [10.1109/ASMC.2017.7969241](#).
- [14] L. Jastrzebski *et al.*, "Review of applications of defect photoluminescence imaging (DPLI) during IC processing," in *Proc. 19th Int. Workshop Junction Technol. (IWJT)*, 2019, pp. 1–6, doi: [10.23919/IWJT.2019.8802893](#).
- [15] R. Duru *et al.*, "Photoluminescence imaging for buried defects detection in silicon: Assessment and use-cases," *IEEE Trans. Semicond. Manuf.*, vol. 32, no. 1, pp. 23–30, Feb. 2019, doi: [10.1109/TSM.2018.2871967](#).
- [16] T. Nakazawa and D. V. Kulkarni, "Wafer map defect pattern classification and image retrieval using convolutional neural network," *IEEE Trans. Semicond. Manuf.*, vol. 31, no. 2, pp. 309–314, May 2018, doi: [10.1109/TSM.2018.2795466](#).
- [17] J. Wang, Z. Yang, J. Zhang, Q. Zhang, and W.-T. K. Chien, "AdaBalGAN: An improved generative adversarial network with imbalanced learning for wafer defective pattern recognition," *IEEE Trans. Semicond. Manuf.*, vol. 32, no. 3, pp. 310–319, Aug. 2019, doi: [10.1109/TSM.2019.2925361](#).
- [18] K. Imoto, T. Nakai, T. Ike, K. Haruki, and Y. Sato, "A CNN-based transfer learning method for defect classification in semiconductor manufacturing," in *Proc. Int. Symp. Semicond. Manuf. (ISSM)*, 2018, pp. 1–3, doi: [10.1109/ISSM.2018.8651174](#).
- [19] "Methods." [Online]. Available: <https://paperswithcode.com/methods> (Accessed: Apr. 2022).
- [20] O. Ronneberger, P. Fischer, and T. Brox, "U-net: Convolutional networks for biomedical image segmentation," in *Proc. Int. Conf. Med. Image Comput. Comput.-Assist. Interv.*, 2015, pp. 234–241.
- [21] A. F. Agarap, "Deep learning using rectified linear units (ReLU)," 2018, *arXiv:1803.08375*.
- [22] D. P. Kingma and J. Ba, "Adam: A method for stochastic optimization, 2014," *arXiv:1412.6980*.
- [23] T.-Y. Lin, P. Goyal, R. Girshick, K. He, and P. Dollár, "Focal loss for dense object detection," in *Proc. IEEE Int. Conf. Comput. Vis. (ICCV)*, 2017, pp. 2999–3007, doi: [10.1109/ICCV.2017.324](#).